



Engineering of layered iron vanadate nanostructure for electrocatalysis: Simultaneous detection of methotrexate and folic acid in blood serum

Kayode Omotayo Adeniyi^{a,*}, Blerina Osmanaj^{a,b}, Gopinathan Manavalan^a,
Ajaikumar Samikannu^a, Jyri-Pekka Mikkola^{a,c}, Berisha Avni^b, Jean-François Boily^a,
Solomon Tesfalidet^{a,*}

^a Department of Chemistry, Umeå University, Umeå 90187, Sweden

^b Department of Chemistry, University of Prishtina, Prishtina 10000, Kosovo

^c Industrial Chemistry and Reaction Engineering, Johan Gadolin Process Chemistry Centre, Åbo Akademi University, Åbo-Turku 20500, Finland

ARTICLE INFO

Keywords:

Iron vanadate
Voltammetric sensor
Electrocatalysts
Therapeutic drug monitoring
Methotrexate
Folic acid

ABSTRACT

In this study, nanostructure kazakhstanite-like iron vanadate ($\text{Fe}_x\text{V}_{3x}\text{O}_y \cdot \text{H}_2\text{O}$) was synthesized and calcined at different temperatures (100–800 °C) in a nitrogen atmosphere. The material was used to modify screen-printed carbon electrodes to achieve an electrocatalytic effect on the surface. The relationship between calcination conditions and the catalytic performance of the electrode towards the oxidation of chemotherapeutic drugs, including methotrexate (MTX) and folic acid (FA), was studied. Various spectroscopic, microscopic, and electrochemical methods were used to characterize the synthesized materials. The results show that calcination induces changes in the electronic structure, nanostructure morphology, electroactive surface area, and electrocatalytic performance of the material. Screen-printed carbon electrode modified with $\text{Fe}_x\text{V}_{3x}\text{O}_y$ calcined at 450 °C (SPC/ $\text{Fe}_x\text{V}_{3x}\text{O}_y$ -450) was used to develop a voltammetric sensor for the determination of MTX and FA in blood serum. The response of the SPC/ $\text{Fe}_x\text{V}_{3x}\text{O}_y$ -450 towards the electrooxidation of MTX and FA was the highest in comparison to the bare SPC and SPC/ $\text{Fe}_x\text{V}_{3x}\text{O}_y$ calcined at other temperatures. The SPC/ $\text{Fe}_x\text{V}_{3x}\text{O}_y$ -450 exhibited a linear relationship over a wide concentration range: 0.005–200 μM for MTX and 0.05–200 μM for FA. The detection limit was 2.85 nM for MTX and 7.79 nM for FA. Compared to conventional methods, the SPC/ $\text{Fe}_x\text{V}_{3x}\text{O}_y$ -450 sensor had a short response time (5 min) for simultaneous detection of MTX and FA without signal interferences from coexisting electroactive compounds. The accurate and precise determination of MTX in the presence of FA confirmed the potential clinical applications of SPC/ $\text{Fe}_x\text{V}_{3x}\text{O}_y$ -450 for therapeutic drug monitoring during chemotherapy.

1. Introduction

Methotrexate (MTX) is an antifolate therapeutic drug widely used to treat cancer and auto-immune diseases [1,2]. However, MTX is cytotoxic, causing multiple organ failures and acute nephrotoxicity. It is necessary to monitor the concentration of MTX in human blood serum for timely control of dosage and guided implementation of folic acid (FA) rescue to fit the therapeutic demand of an individual patient and prevent toxicity-related complications [3]. High-performance liquid chromatography (HPLC), fluorescence polarization, chemiluminescent microparticles immunoassay, and homogenous enzyme immunoassays are routinely used to determine MTX [4–6]. However, these assays require complex sample treatment, expensive equipment, and a long

turn-around time, which limits the timely adjustment of MTX dosage and administration of FA. Therefore, a rapid, inexpensive, miniaturized analytical device for real-time monitoring of MTX is an unmet need in clinical chemotherapy.

Electrochemical voltammetric sensors displayed fascinating features for developing highly sensitive and portable bioanalytical sensing systems amenable to point-of-care measurement. The voltammetry transduction principle is based on the direct redox reaction of the biochemical analytes at the interface of a solid electrode. The slow electron transfer kinetics and high overpotential required to initiate this electrochemical process at the bare electrode limit the accuracy and sensitivity of detection. The overpotential leads to poor selectivity and causes unwanted interferences from co-existing analytes [7]. Modifying

* Corresponding authors.

E-mail addresses: omotayo.adeniyi@umu.se (K.O. Adeniyi), solomon.tesfalidet@umu.se (S. Tesfalidet).

<https://doi.org/10.1016/j.electacta.2023.142538>

Received 30 December 2022; Received in revised form 7 April 2023; Accepted 4 May 2023

Available online 5 May 2023

0013-4686/© 2023 The Authors. Published by Elsevier Ltd. This is an open access article under the CC BY license (<http://creativecommons.org/licenses/by/4.0/>).

transducer interfaces with nanostructured electrocatalytic materials has great potential to overcome these challenges. Electrochemical transducer interfaces modified with nanostructured ternary transition metal vanadate ($M_xV_yO_z$, $M = Cu, Ni, Co, Fe$) [8–12] are of interest in various electrocatalytic applications dedicated to biochemical sensing due to their tunable electrocatalytic properties, electronic bandgap, and natural abundance [12]. Among the various $M_xV_yO_z$, iron vanadate ($Fe_xV_yO_z$) has excellent electrocatalytic activity due to the synergistic strong electron-electron correlation of the multi-valent oxidation states of Fe ions (Fe^{2+} to Fe^{+6}) and vanadium ions (V^{2+} to V^{5+}) [13]. Compared to amorphous $FeVO_4$ nanoparticles [10–12,14], kazakhstanite ($Fe_5V_{15}O_{39}(OH)_9 \cdot 9H_2O$) is a hydrated layered crystalline compound with high ionic conductivity and a large surface area [15–17]. However, the intrinsic poor electrical conductivity of $Fe_xV_{3x}O_y \cdot zH_2O$ limit its electrocatalytic sensing applications.

In this study, we present the first report on engineering $Fe_xV_{3x}O_y$ structural morphology, crystalline facet, and oxygen vacancy via calcination at different temperatures to yield oxygen-deficient dehydrated $Fe_xV_{3x}O_y$ nanostructures. $Fe_xV_{3x}O_y$ modified carbon screen-printed electrode was fabricated and utilized for the voltammetric determination of MTX and FA in human blood serum. The influence of changes in the physicochemical properties and electrocatalytic performance of $Fe_xV_{3x}O_y$ towards MTX and FA was investigated. The prepared $Fe_xV_{3x}O_y$ catalysts were characterized using various microscopic and spectroscopic techniques. The novelty of this study includes: (i) providing information on the influence of calcination temperature on the morphology, crystallinity, surface-active redox species, oxygen vacancies, and electrochemical properties of dehydrated $Fe_xV_{3x}O_y$, (ii) developing an ultrasensitive electrochemical sensor based on $Fe_xV_{3x}O_y$ -modified electrodes for the simultaneous detection of MTX and FA in human clinical serum sample reported for the first time.

2. Experimental

All reagents and solvents were of analytical grade. The detail about the reagent supplies and instrumental analysis procedures are reported in the supporting information (SI).

2.1. Preparation of $Fe_xV_{3x}O_y$ nanostructured electrocatalysts

The synthesis of hydrated layered $Fe_xV_{3x}O_y \cdot zH_2O$ nanosheet was achieved by co-precipitation from an aqueous mixture of 90 ml of Fe

$(NO_3)_3 \cdot 9H_2O$ (1.2 g, 2.85 mmol) and 10 ml of NH_4VO_3 (1.0 g, 8.55 mmol) heated at 100 °C for 24 hrs (Fig. 1a). The color of the solution changed from yellow to a brown precipitate. The brown $Fe_xV_{3x}O_y \cdot zH_2O$ precipitate was separated by centrifugation, washed with deionized water and ethanol, and dried at 60 °C in a vacuum oven. The synthesized $Fe_xV_{3x}O_y \cdot zH_2O$ (0.2 g) was calcined at different temperatures ($T = 300, 450, 600, \text{ and } 800$ °C) at a heating rate of 5 °C/min for 4 hrs in a tube furnace under a flowing stream of nitrogen gas flow. The powdered product obtained after calcination was generally referred to as $Fe_xV_{3x}O_y$ -T and designated as $Fe_xV_{3x}O_y$ -300, $Fe_xV_{3x}O_y$ -450, $Fe_xV_{3x}O_y$ -600, and $Fe_xV_{3x}O_y$ -800 corresponding to calcination at (T) = 300, 450, 600 and 800 °C, respectively.

2.2. Fabrication of SPC- $Fe_xV_{3x}O_y$ -T electrodes

The $Fe_xV_{3x}O_y$ -T (10.0 mg) were dispersed in deionized water (5.0 mL) and ultrasonicated for 60 mins. Screen-printed carbon electrodes (SPCEs) were used as substrate and subjected to electrochemical cleaning by cyclic voltammetry treatment between -0.8 and 1.1 V vs. Ag-SPE in 0.5 M sulphuric acid solution for 10 cycles. The SPCEs were rinsed with H_2O and dried with a flowing nitrogen gas (N_2) stream. The $Fe_xV_{3x}O_y$ -T inks (10.0 μ L, 2.0 mg. mL^{-1}) were then dropped onto the circular working electrode area of the cleaned SPCEs and allowed to dry at room temperature. The dried $Fe_xV_{3x}O_y$ -T inks form a stable thin film on the carbon electrode without adding a binder. The individually modified SPC/ $Fe_xV_{3x}O_y$ -T electrodes were rinsed with Milli-Q water and stored at room temperature.

3. Results and discussion

3.1. Composition and structure of $Fe_xV_{3x}O_y$ -T

The preparation process of $Fe_xV_{3x}O_y$ -T with various nanostructures is illustrated in Fig. 1. The calcination of prepared hydrated $Fe_xV_{3x}O_y \cdot zH_2O$ in an inert atmosphere could induce recrystallization, defects, and facet changes, influencing the physicochemical and catalytic properties [18]. The calcined-powdered products showed different physical color appearances depending on the calcination temperatures (Fig. 1b). The brown $Fe_xV_{3x}O_y \cdot zH_2O$ powder changed to varying shades of light green at calcination temperatures of 300 °C ($Fe_xV_{3x}O_y$ -300) and 450 °C ($Fe_xV_{3x}O_y$ -450), yellowish green at 600 °C ($Fe_xV_{3x}O_y$ -650), and blue-black at 800 °C ($Fe_xV_{3x}O_y$ -800).

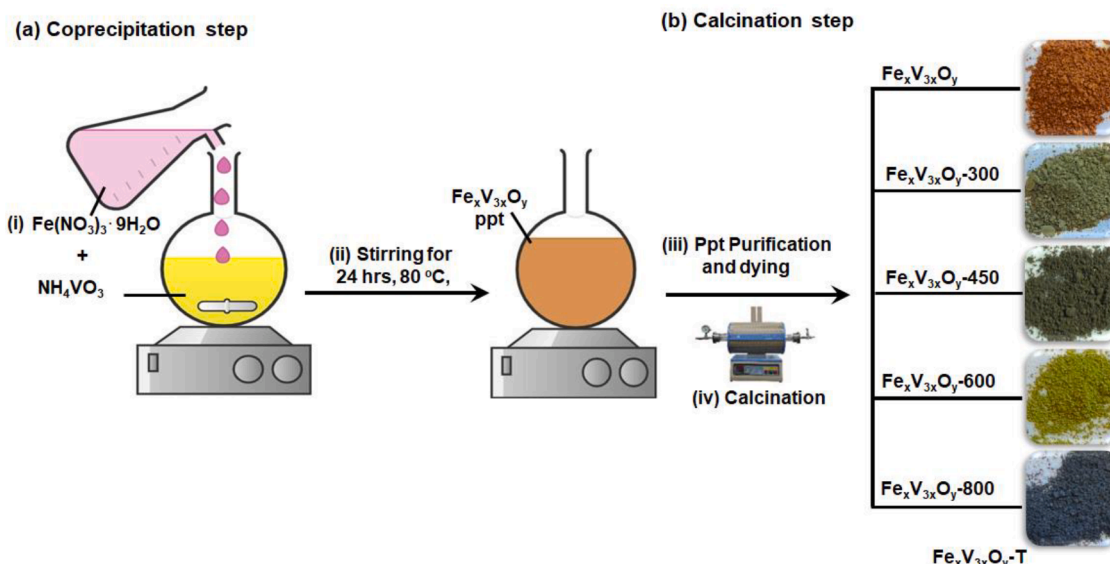


Fig. 1. Schematic illustration of the preparation of different $Fe_xV_{3x}O_y$ -T electrocatalyst.

The color changes in the calcined samples are attributed to changes in the absorption band edges due to the temperature-dependent reduction of vanadium and iron to their different metastable oxidation states. The UV-Vis diffuse reflectance spectra (UV-Vis DRS) of $\text{Fe}_x\text{V}_{3x}\text{O}_y \cdot z\text{H}_2\text{O}$ (Fig. 2a-i) shows reflection bands in the ultraviolet (250–330 nm), violet-blue (330–399), and orange-red (580–750 nm) regions of the visible spectra. These reflections are characteristic of the d-d transition of various V-O (V^{4+} , V^{5+}) and Fe-O (Fe^{2+} and Fe^{3+}) species, and the mixture resulted in the brown color of $\text{Fe}_x\text{V}_{3x}\text{O}_y \cdot z\text{H}_2\text{O}$. The decrease in reflectance observed between 400 and 550 nm corresponds to the onset of the adsorption due to electronic transition across the band gap. The $\text{Fe}_x\text{V}_{3x}\text{O}_y \cdot z\text{H}_2\text{O}$ has an indirect band gap of 2.2 eV (Fig S1, i). The reflectance intensity in the orange-red region decreased significantly

after calcination (Fig. 2a, i-iv). $\text{Fe}_x\text{V}_{3x}\text{O}_y$ -300, $\text{Fe}_x\text{V}_{3x}\text{O}_y$ -450, and $\text{Fe}_x\text{V}_{3x}\text{O}_y$ -600 showed reflection in the violet-blue and green-yellow regions due to Fe^{2+} , V^{3+} , and V^{4+} and V^{4+} ions. The combinations of reflectance from different mixes of these ions resulted in different shades of greenish color. Initially, the bandgap increased from 2.2 eV for $\text{Fe}_x\text{V}_{3x}\text{O}_y \cdot z\text{H}_2\text{O}$ to 3.18 eV for $\text{Fe}_x\text{V}_{3x}\text{O}_y$ -300 and 3.35 eV for $\text{Fe}_x\text{V}_{3x}\text{O}_y$ -450. However, with a further increase in calcination temperature, the bandgap decreased to 2.8 eV for $\text{Fe}_x\text{V}_{3x}\text{O}_y$ -600 and 2.3 eV for $\text{Fe}_x\text{V}_{3x}\text{O}_y$ -800. Calcination causes the loss of hydrated water in the crystalline structure, which could result in the modification of the electronic structure and the number of the electronic state, leading to an increase in the band gap energy [19].

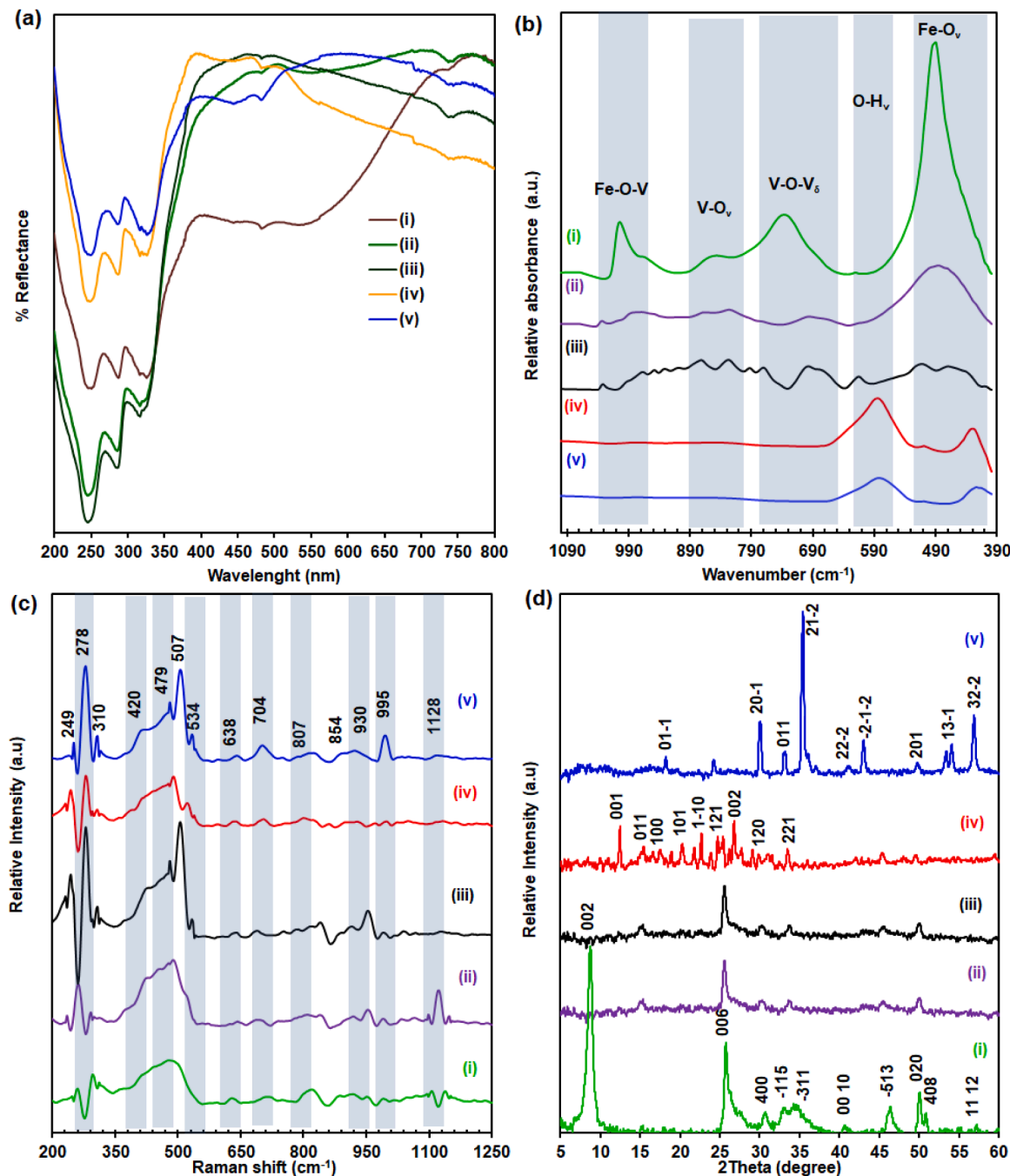


Fig. 2. (a) DRS (b) FTIR spectra, (c) Raman spectra, and (d) XRD patterns of (i) $\text{Fe}_x\text{V}_{3x}\text{O}_y \cdot z\text{H}_2\text{O}$, (ii) $\text{Fe}_x\text{V}_{3x}\text{O}_y$ -300, (iii) $\text{Fe}_x\text{V}_{3x}\text{O}_y$ -450, (iv) $\text{Fe}_x\text{V}_{3x}\text{O}_y$ -600, and (v) $\text{Fe}_x\text{V}_{3x}\text{O}_y$ -800.

3.1.1. Elemental mapping

The EDS spectra of $\text{Fe}_x\text{V}_{3-x}\text{O}_y \cdot \text{zH}_2\text{O}$ before (Fig.S2, a) and after calcination (Fig.S2, b-e) confirmed the presence of Fe, V, and O. EDS elemental mapping (Fig. S3) also confirmed the homogeneous distribution of Fe, V, and O in all samples. The EDS atomic composition (inset of Fig.S3, a-e) and elemental analysis by ICP-OES (Table S1) for samples calcined below 800 °C revealed an average vanadium-to-iron atomic ratio (V/Fe) of -3.3:1, which is close to that of the ferric nitrate and ammonium vanadate precursors (3:1). The V/Fe ratio of the same calcined at 800 °C was however lowered to -2:1, indicating the volatilization of vanadium at a higher temperature.

3.1.2. Fe-O and V-O bonding

The FTIR spectra of $\text{Fe}_x\text{V}_{3-x}\text{O}_y \cdot \text{zH}_2\text{O}$ before calcination (Fig.S4, i) revealed the existence of adsorbed water molecules ($\text{O}-\text{H}_{\text{vs}}$ at 3575 cm^{-1} ; $(\text{H}_2\text{O})_6$ at 1633 cm^{-1}) and structural water of hydration ($\text{O}-\text{H}_{\text{ls}}$ at 3215 cm^{-1} ; $(\text{H}_2\text{O})_6$ at 1608 cm^{-1}). However, calcination removed adsorbed water from all samples at >100 °C (Fig.S4, ii-v), confirming the formation of dehydrated $\text{Fe}_x\text{V}_{3-x}\text{O}_y$. The metal oxide vibrations (Fig. 2b, ii-v) confirmed the Fe-O stretching (489–424 cm^{-1}), V=O stretching, and Fe-O-V bending vibrations (1008 cm^{-1}) [20]. The bands between 732 and 1031 cm^{-1} were attributed to the vanadyl bonds (V-O-V, V-O) stretching and bending vibrations [21]. However, the intensity of the Fe-O and O-V-O bonds decreased and shifted to lower wavenumbers as the calcination temperature increased. The lower intensity and the blue shift could be associated with shorter Fe-O and V-O bond lengths. The Fe-O and V-O interactions were resolved further by Raman spectroscopy (Fig. 1c). Peaks at the lowest vibrational frequencies (200–300 cm^{-1}) are attributed to Fe-O, O-V-O, and V-O-Fe mixed bending and torsion modes vibrations. The broad V-O...Fe and V...O...Fe bridging (420–550 cm^{-1}) [22] and terminal V-O stretching (848–930 cm^{-1}) vibrations [13] showed that oxygen atoms were mainly located at bridging and terminal positions. The main difference in the Raman spectra is the redshift and splitting of the broad band between 350 and 550 cm^{-1} into well-resolved and intense spectra lines with increasing calcination temperature (Fig. 2c, i-v). The peak at 704 cm^{-1} (Fe-O stretching) in all the samples before and after calcination aligns with binding with Fe^{3+} ions, and the emergence of a new band at 534 cm^{-1} (Fe-O stretching) after calcination at high temperatures (≥ 450 °C) confirms the reduction to Fe^{2+} during the calcination process [23]. Also, the blue shift and lower intensity of the $\text{V}^{5+}=\text{O}$ bonds stretching vibrations (128 cm^{-1}) with increasing calcination temperatures indicated higher oxygen deficiency (Fig. 2c, i-v).

3.1.3. Phase identification

XRD pattern of $\text{Fe}_x\text{V}_{3-x}\text{O}_y \cdot \text{zH}_2\text{O}$ before calcination (Fig. 2d, i) corresponds to the monoclinic crystalline phase of pure layered iron-vanadium hydrate ($\text{Fe}_5^{3+}\text{V}_3^{5+}\text{V}_2^{5+}\text{O}_{39}(\text{OH})_9 \cdot 9\text{H}_2\text{O}$, known as kazakhstanite), (JCPDS No. 46–1334) [15]. The $\text{Fe}_x\text{V}_{3-x}\text{O}_y$ -300 and $\text{Fe}_x\text{V}_{3-x}\text{O}_y$ -450 showed similar diffraction peaks to $\text{Fe}_x\text{V}_{3-x}\text{O}_y \cdot \text{zH}_2\text{O}$ except for the absence of the (002) crystallographic plane and lower peak intensities (Fig. 2d, ii-iii). The absence of the (002) crystallographic planes and lowered peak intensities indicate a loss of crystalline water molecules and an increase in amorphous character. New diffraction peaks ($2\theta = 12.71^\circ$ to 33.73°) corresponding to triclinic FeV_3O_8 (JCPDS No. 36–0007) appeared in $\text{Fe}_x\text{V}_{3-x}\text{O}_y$ -600 (Fig. 2d, iii). The $\text{Fe}_x\text{V}_{3-x}\text{O}_y$ decomposed at ≥ 450 °C and recrystallized in the triclinic P1 space group of triclinic FeV_3O_8 at 600 °C ($\text{Fe}_x\text{V}_{3-x}\text{O}_y$ -600). The crystalline structure confirms the coordination environment of V^{5+} , Fe^{3+} , V^{4+} and O^{2-} in $\text{Fe}_x\text{V}_{3-x}\text{O}_y$ -600. However, the XRD pattern of $\text{Fe}_x\text{V}_{3-x}\text{O}_y$ -800 (Fig. 2d, v) indicated the formation of the triclinic crystalline phase of FeV_2O_4 with a P1 space group (JCPDS No. 01–075–0317) after calcination at 800 °C. The coordination environment confirmed Fe^{2+} , Fe^{3+} , V^{3+} and O^{2-} oxidation states in $\text{Fe}_x\text{V}_{3-x}\text{O}_y$ -800.

3.1.4. Particle morphology

FE-SEM (Fig. 3) and TEM images (Fig. 4) revealed differences in morphology and microstructure after calcination. The $\text{Fe}_x\text{V}_{3-x}\text{O}_y$ before calcination showed layered flake-like morphology with wrinkles and rough edges. After calcination at 300 °C, the $\text{Fe}_x\text{V}_{3-x}\text{O}_y$ -300 exhibited crumpled nanoflake-like morphology with smaller particle sizes than $\text{Fe}_x\text{V}_{3-x}\text{O}_y \cdot \text{zH}_2\text{O}$ (Fig. 3b). The nanoflake-like $\text{Fe}_x\text{V}_{3-x}\text{O}_y$ self-assembled into the agglomerated oval microflower structure after calcination at 450 °C ($\text{Fe}_x\text{V}_{3-x}\text{O}_y$ -450, Fig. 3c) to reduce the surface energy. The $\text{Fe}_x\text{V}_{3-x}\text{O}_y$ -600 (Fig. 3d) showed a mixture of rectangular multilayered sheets and some irregular truncated polyhedron particles, indicating Ostwald ripening [24,25] and recrystallization of $\text{Fe}_x\text{V}_{3-x}\text{O}_y$ occurred at $450 \leq T \leq 600$ °C. The formation of truncated irregular octahedron nanoparticles with well-defined edges and smooth surfaces was observed by FE-SEM of $\text{Fe}_x\text{V}_{3-x}\text{O}_y$ -800 (Fig. 3e). TEM images (Fig. 4a–e, II) also confirmed morphological changes through the formation of two-dimensional micrometer-wide and nanometer-thick $\text{Fe}_x\text{V}_{3-x}\text{O}_y$ -300 nanoflakes, $\text{Fe}_x\text{V}_{3-x}\text{O}_y$ -450 nanoflower, and $\text{Fe}_x\text{V}_{3-x}\text{O}_y$ -600 rectangular nanosheet. HRTEM images (Fig. 4a–e, ii) and the inverse fast Fourier transform (IFFT) atomic lattice images (inset Fig. 4a–e, III) revealed well-defined lattice fringes implying a crystalline structure as observed with the XRD result. A lattice d-spacing of -0.92 nm, consistent with the interlayer spacing of the (002) crystalline plane, was predominant in the $\text{Fe}_x\text{V}_{3-x}\text{O}_y \cdot \text{zH}_2\text{O}$ before calcination. Two intersecting planes with a d-spacing of -0.35 nm and 0.28 nm were observed in the $\text{Fe}_x\text{V}_{3-x}\text{O}_y$ -300 and $\text{Fe}_x\text{V}_{3-x}\text{O}_y$ -450, implying that growth, respectively proceeded along the (204) and (115) crystal planes. The changes in the lattice distance to 0.56 nm (001 crystal plane) after calcination at 600 °C and 0.43 nm (001 crystal plane) confirmed recrystallization and formation of FeV_3O_8 and after calcination at 800 °C of FeV_2O_4 . Also, disorder and edge dislocation defects were observed in the lattice fringes (red cycled regions in Fig. 4b–e, (IV)), confirming the presence of rich crystalline oxygen vacancies in the calcined $\text{Fe}_x\text{V}_{3-x}\text{O}_y$.

3.1.5. Surface area and microporosity

The Nitrogen (N_2) adsorption-desorption isotherms (Fig.S6) showed a type IV isotherm with a sharp knee at a relative pressure between 0.85 and 1.0. The isotherms exhibited an H3-type hysteresis loop, and no plateau was observed at the highest relative pressures, which correlates to the presence of slit-shaped mesopores according to the IUPAC classification [26]. The surface area was calculated using the Brunauer-Emmett-Teller method (BET) [27] by an in-built software from Micromeritics. Detailed information is available in the supplementary (SI). The BET surface area (S_{BET}) increased from 38.27 m^2g^{-1} for $\text{Fe}_x\text{V}_{3-x}\text{O}_y \cdot \text{zH}_2\text{O}$ to 53.74 m^2g^{-1} and 48.68 m^2g^{-1} when calcined at 300 °C ($\text{Fe}_x\text{V}_{3-x}\text{O}_y$ -300) and 450 °C ($\text{Fe}_x\text{V}_{3-x}\text{O}_y$ -450), respectively. Removing impurities and adsorbed water molecules could be responsible for the increased surface area. The significant decrease in S_{BET} to 5.47 m^2g^{-1} for $\text{Fe}_x\text{V}_{3-x}\text{O}_y$ -600 and 4.14 m^2g^{-1} for $\text{Fe}_x\text{V}_{3-x}\text{O}_y$ -800 (Table S2) resulted from the destruction of pore structures and increased crystallinity. The steep N_2 absorption at the beginning ($P/P_0 < 0.1$) in the isotherm of $\text{Fe}_x\text{V}_{3-x}\text{O}_y$ -600 and $\text{Fe}_x\text{V}_{3-x}\text{O}_y$ -800 could be ascribed to the presence of micropores. A t-plot analysis [28] (Fig. 5) showed that $\text{Fe}_x\text{V}_{3-x}\text{O}_y \cdot \text{zH}_2\text{O}$ has a microporosity of -2.3 $\mu\text{L.g}^{-1}$. Calcination at 300 °C caused a slight increase to -3.7 $\mu\text{L.g}^{-1}$, and this microporosity collapsed to -1.0 $\mu\text{L.g}^{-1}$ at higher calcination temperatures (600–800 °C). The microchannels expelling water vapor during thermal dehydration and dehydroxylation explain the slight increase in microporosity at $\text{Fe}_x\text{V}_{3-x}\text{O}_y$ -300 °C and $\text{Fe}_x\text{V}_{3-x}\text{O}_y$ -450 °C, which aligns with the loss of structural crystalline water. At higher temperatures, recrystallization collapsed this microporosity. The $\text{Fe}_x\text{V}_{3-x}\text{O}_y \cdot \text{zH}_2\text{O}$, $\text{Fe}_x\text{V}_{3-x}\text{O}_y$ -300, and $\text{Fe}_x\text{V}_{3-x}\text{O}_y$ -450 had a micropore volume of 0.17, 0.31 and 0.35 cm^3g^{-1} , respectively. The $\text{Fe}_x\text{V}_{3-x}\text{O}_y$ -600 and $\text{Fe}_x\text{V}_{3-x}\text{O}_y$ -800 had a ten-time lower pore volume of 0.015 and 0.020 cm^3g^{-1} , respectively. The average pore diameter increased from 17.7 nm for $\text{Fe}_x\text{V}_{3-x}\text{O}_y \cdot \text{zH}_2\text{O}$ to 26.04 nm for $\text{Fe}_x\text{V}_{3-x}\text{O}_y$ -300. Then, a progressive decrease in the pore size diameter to

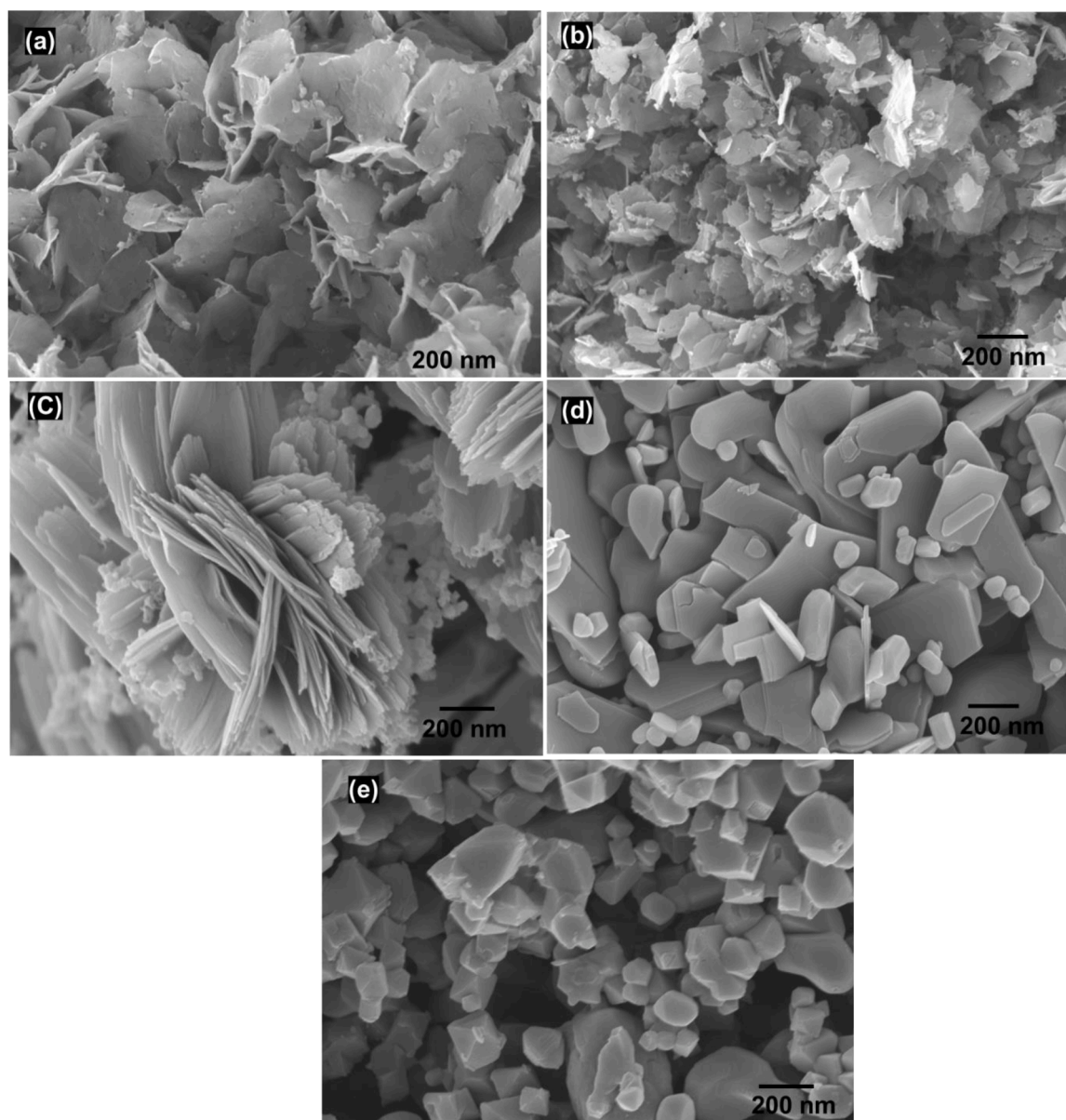


Fig. 3. FE-SEM images of (a) $\text{Fe}_x\text{V}_{3x}\text{O}_y \cdot z\text{H}_2\text{O}$, (b) $\text{Fe}_x\text{V}_{3x}\text{O}_y$ -300, (c) $\text{Fe}_x\text{V}_{3x}\text{O}_y$ -450, (d) $\text{Fe}_x\text{V}_{3x}\text{O}_y$ -600, and (e) $\text{Fe}_x\text{V}_{3x}\text{O}_y$ -800.

10.8 and 8.4 nm was observed with increasing calcination temperature from 600 to 800 °C. The decrease in the pore size diameter is attributed to an increase in crystallinity and changes in the structural morphology at higher calcination temperatures (≥ 450 °C), as seen in the XRD and HRTEM analysis.

3.1.6. Surface composition and (Fe, V) oxidation states

XPS analysis revealed the $\text{Fe}_x\text{V}_{3x}\text{O}_y \cdot z\text{H}_2\text{O}$ surface atom composition, elemental binding sites, and changes in oxidation states before and after calcination at different temperatures. The survey scan in Fig. S7 confirmed the Fe, V, O, C, and N atoms in all the samples. The high-resolution Fe 2p core-level spectra (Fig. 6a) showed a broad split spin-orbit doublet with characteristic satellite peaks attributed to the photoemission of Fe 2p_{3/2} and Fe 2p_{1/2} species. The spin-orbit constant (ΔBE) between the Fe 2p_{3/2} and Fe 2p_{1/2} (13.5 eV) was close to the standard value for iron oxide (13.0 eV) species [29]. The broad Fe 2p_{3/2} spectra of $\text{Fe}_x\text{V}_{3x}\text{O}_y$ before and after calcination at different temperatures were deconvoluted into three components with repeated patterns of half intensity for the Fe 2p_{1/2} spectra. The BE at 710.7 eV confirms the

existence of Fe^{2+} ions, while the peak at 712.5 and 715.3 eV were due to the octahedral and tetrahedral coordinated Fe^{3+} ions. The BE of Fe^{2+} and Fe^{3+} ions shifted towards higher values with increasing calcination temperatures from 300 to 800 °C. The higher BE shifts imply an increased shielding of the Fe cation by electronegative (V-O) ligands [30], implying an increase in the degree of the ionic bond character of the Fe-V-O bond. The high-resolution V 2p spectrum of $\text{Fe}_x\text{V}_{3x}\text{O}_y$ before calcination showed a single spin-orbit doublet at 517.5 eV ($\text{V}^{5+}2\text{p}_{3/2}$) and 525.1 eV ($\text{V}^{5+}2\text{p}_{1/2}$) of V^{+5} (Fig. 6c, i). Before calcination, the V atoms predominately exist in the (+5)-oxidation state in the $\text{Fe}_x\text{V}_{3x}\text{O}_y \cdot z\text{H}_2\text{O}$. Notably, after calcination, the V2p spectrum of FeV_3O_y -300 and FeV_3O_y -450 showed an additional pair of doublets attributed to the V^{4+} ions at 516.4 eV ($\text{V}^{4+}2\text{p}_{3/2}$) and 523.6 eV ($\text{V}^{4+}2\text{p}_{1/2}$) (Fig. 6c, ii and iii). The $\text{Fe}_x\text{V}_{3x}\text{O}_y$ -600 and $\text{Fe}_x\text{V}_{3x}\text{O}_y$ -800 showed a third component attributed to V^{3+} ions at 515.4 eV ($\text{V}^{3+}2\text{p}_{3/2}$) and 523.4 eV ($\text{V}^{3+}2\text{p}_{1/2}$). The lower oxidation state indicated that more electrons were injected into the 3d-orbital of vanadium during the oxygen-deficient calcination process. The O1s spectra of $\text{Fe}_x\text{V}_{3x}\text{O}_y \cdot z\text{H}_2\text{O}$ and $\text{Fe}_x\text{V}_{3x}\text{O}_y$ -300 were deconvoluted into three components, while the $\text{Fe}_x\text{V}_{3x}\text{O}_y$ -450,

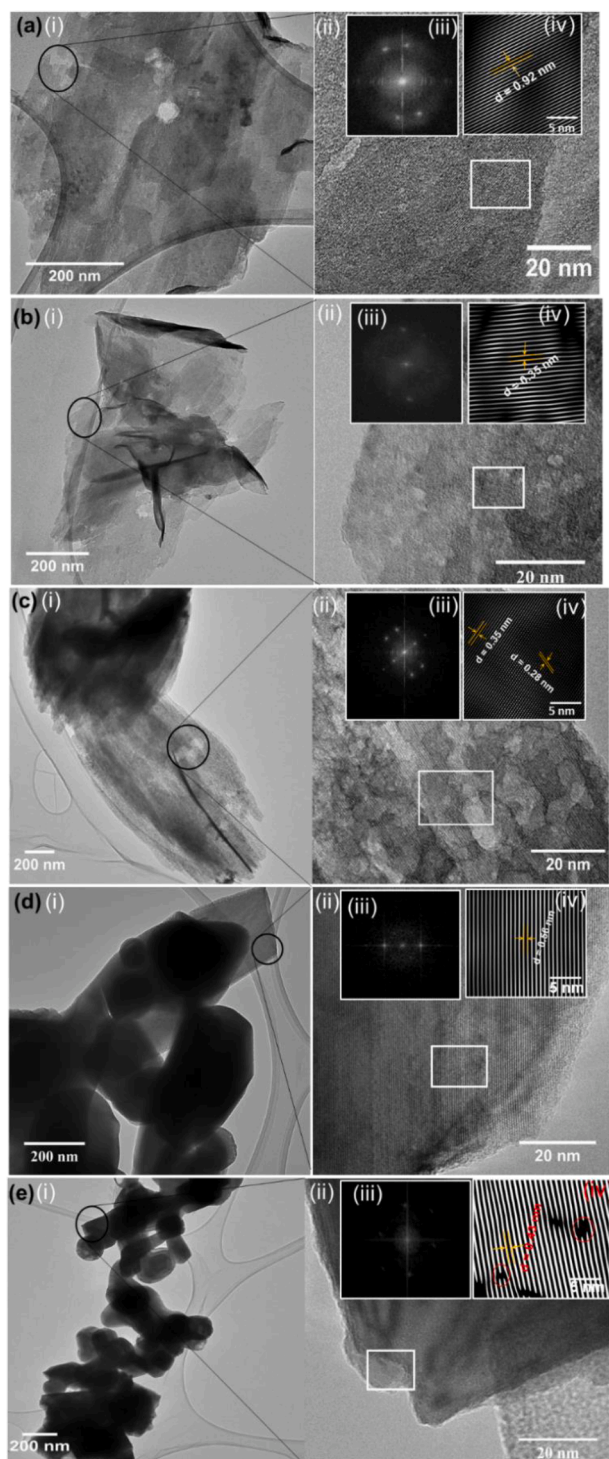


Fig. 4. (i) TEM images, (ii) HRTEM, (iii) FFT, and (iv) inverse FFT with d-spacing from HRTEM images of (a) $\text{Fe}_x\text{V}_{3x}\text{O}_y.\text{zH}_2\text{O}$, (b) $\text{Fe}_x\text{V}_{3x}\text{O}_y\text{-300}$, (c) $\text{Fe}_x\text{V}_{3x}\text{O}_y\text{-450}$, (d) $\text{Fe}_x\text{V}_{3x}\text{O}_y\text{-600}$, and (e) $\text{Fe}_x\text{V}_{3x}\text{O}_y\text{-800}$.

$\text{Fe}_x\text{V}_{3x}\text{O}_y\text{-600}$, and $\text{Fe}_x\text{V}_{3x}\text{O}_y\text{-800}$ were deconvoluted into two components. The O1s peak at -530.4 and -531.3 eV corresponds to the Fe-O and V-O bonds surface lattice oxygen (O_{lat}) [31]. The absence of hydroxyl oxygen (O_{OH}) in the calcined samples resulted from thermal dehydroxylation.

A slight shift of O 1s towards lower BE with increasing temperature indicates a new oxygen chemical environment. The value of $(\text{V}^{4+} + \text{V}^{3+})/\text{V}^{5+}$ and oxygen vacancy ($\text{O}_{\text{ads}}/(\text{O}_{\text{lat}} + \text{O}_{\text{ads}})$) influences the catalytic activity [32]. Where oxygen (O_{ads}) is the adsorbed oxygen species.

The relative atomic percentage ratio of ($\text{O}_{\text{ads}}/(\text{O}_{\text{lat}} + \text{O}_{\text{ads}})$) indicated the concentration of the oxygen vacancies. The $\text{Fe}_x\text{V}_{3x}\text{O}_y.\text{zH}_2\text{O}$ presented a relative oxygen vacancy ($\text{O}_{\text{ads}}/(\text{O}_{\text{lat}} + \text{O}_{\text{ads}})$) concentration of 9.7%, which increased to 11.7% for $\text{Fe}_x\text{V}_{3x}\text{O}_y\text{-300}$ and $\text{Fe}_x\text{V}_{3x}\text{O}_y\text{-450}$, 8.7% for $\text{Fe}_x\text{V}_{3x}\text{O}_y\text{-600}$ and 20.3% for $\text{Fe}_x\text{V}_{3x}\text{O}_y\text{-800}$. The higher concentrations of ($\text{O}_{\text{ads}}/(\text{O}_{\text{lat}} + \text{O}_{\text{ads}})$) confirmed the formation of oxygen vacancies with increasing calcination temperature. The relative atomic ratio of V/Fe at the surface of $\text{Fe}_x\text{V}_{3x}\text{O}_y.\text{zH}_2\text{O}$ (2.2: 1) was lower than the bulk atomic V/Fe ratio (3.2:1) from ICP-OES analysis. The lower ratio showed that Fe relative to V atoms is abundant on the surface of the FeV_3O_y after calcination. The increase in V/Fe ratios after calcination is attributed to the enrichment of reduced V-O at the surface of the FeV_3O_y . The value of $(\text{V}^{4+} + \text{V}^{3+})/\text{V}^{5+}$ ratios increased with increasing calcination temperature from 0.18 for $\text{Fe}_x\text{V}_{3x}\text{O}_y\text{-300}$ to 0.31 for $\text{Fe}_x\text{V}_{3x}\text{O}_y\text{-800}$. This increase indicated that more V^{5+} were reduced to V^{4+} and V^{3+} with increasing calcination temperature under the nitrogen atmosphere.

3.2. Electrochemical properties of SPC/ $\text{Fe}_x\text{V}_{3x}\text{O}_y\text{-T}$ electrodes

The SPC/ $\text{Fe}_x\text{V}_{3x}\text{O}_y.\text{zH}_2\text{O}$ and SPC/ $\text{Fe}_x\text{V}_{3x}\text{O}_y\text{-T}$ electrodes were characterized using cyclic voltammetry (CV) and electrochemical impedance spectroscopy (EIS) in aqueous $[\text{Fe}(\text{CN})_6]^{3-/4-}$ redox electrolyte containing 0.1 M KCl (Fig.S8). The cyclic voltammograms in Fig. S8a showed good reversibility for the redox process of $[\text{Fe}(\text{CN})_6]^{3-/4-}$ on the SPC/ $\text{Fe}_x\text{V}_{3x}\text{O}_y\text{-T}$. The redox peak current density was higher at the modified SPC/ $\text{Fe}_x\text{V}_{3x}\text{O}_y\text{-T}$ electrodes than at the unmodified SPC electrode (Fig.S8a, ii-iv). The intensity of the redox peak current is proportional to the electroactive surface area (E_{SA}) of the different SPC/ $\text{Fe}_x\text{V}_{3x}\text{O}_y\text{-T}$ electrodes and was calculated from the Randle-Sevick relationship (Eq. (1)) [33].

$$E_{\text{SA}} = \frac{I_p}{k \cdot n^{3/2} \cdot A \cdot D^{1/2} \cdot C \cdot \nu^{1/2}} \quad (1)$$

: where I_p is the magnitude of the anodic or cathodic peak current, $k = 2.72 \times 10^5$, n is the number of electrons transferred ($n = 1$), D is the diffusion coefficient ($7.6 \times 10^{-10} \text{ m}^2 \cdot \text{s}^{-1}$), C is the concentration of $[\text{Fe}(\text{CN})_6]^{3-/4-}$ (2.0 mM), and ν is the scan rate (0.05 V/s).

The SPC/ $\text{Fe}_x\text{V}_{3x}\text{O}_y\text{-300}$ and SPC/ $\text{Fe}_x\text{V}_{3x}\text{O}_y\text{-450}$ had higher electroactive surface area than the SPC/ $\text{Fe}_x\text{V}_{3x}\text{O}_y.\text{zH}_2\text{O}$, SPC/ $\text{Fe}_x\text{V}_{3x}\text{O}_y\text{-650}$, and SPC/ $\text{Fe}_x\text{V}_{3x}\text{O}_y\text{-800}$. The SPC/ $\text{Fe}_x\text{V}_{3x}\text{O}_y\text{-450}$ and SPC/ $\text{Fe}_x\text{V}_{3x}\text{O}_y\text{-300}$ showed excellent electrochemical properties due to the synergistic effect of their two-dimensional morphology, high electroactive surface area, high pore volume, and pore diameter that endowed them with faster ion diffusion and rapid charge transfer properties.

Electrochemical impedance spectroscopy was used to evaluate the electrochemical reaction kinetics and charge transfer properties of the various SPC/ $\text{Fe}_x\text{V}_{3x}\text{O}_y\text{-T}$ electrode. Fig.S8b, ii-iv compares the Nyquist plots of the bare SPC, SPC/ $\text{Fe}_x\text{V}_{3x}\text{O}_y.\text{zH}_2\text{O}$, and various SPC/ $\text{Fe}_x\text{V}_{3x}\text{O}_y\text{-T}$. The fitted EIS data were summarized in Table S4. The semicircle diameter of the Nyquist plot corresponding to the interface charge transfer resistance (R_{CT}) of the SPC/ $\text{Fe}_x\text{V}_{3x}\text{O}_y\text{-T}$ and uncalcined $\text{Fe}_x\text{V}_3\text{O}_y.\text{zH}_2\text{O}$ were higher than the SPC electrode, indicating the semi-conducting properties of the $\text{Fe}_x\text{V}_{3x}\text{O}_y\text{-T}$. Compared to the uncalcined $\text{Fe}_x\text{V}_3\text{O}_y.\text{zH}_2\text{O}$, the R_{CT} decreased significantly after calcination at 300 to 450 °C (Table S4) and increased at higher temperatures (≥ 600 °C). The lowest R_{CT} of the SPC/ $\text{Fe}_x\text{V}_{3x}\text{O}_y\text{-300}$ and SPC/ $\text{Fe}_x\text{V}_{3x}\text{O}_y\text{-450}$ confirms the higher efficient charge transfer process.

3.3. Electrochemical behavior of MTX and FA at SPC/ $\text{Fe}_x\text{V}_{3x}\text{O}_y\text{-T}$ electrodes

The redox behavior of MTX and FA in phosphate buffer solution (PBS) at SPC/ $\text{Fe}_x\text{V}_{3x}\text{O}_y\text{-T}$ electrodes was investigated using cyclic voltammetry (Fig. 7). The CV of the bare SPC, SPC/ $\text{Fe}_x\text{V}_{3x}\text{O}_y.\text{zH}_2\text{O}$, and SPC/ $\text{Fe}_x\text{V}_{3x}\text{O}_y\text{-T}$ electrodes in the PBS alone did not show redox peaks within the studied potential window. An unresolved broad anodic peak

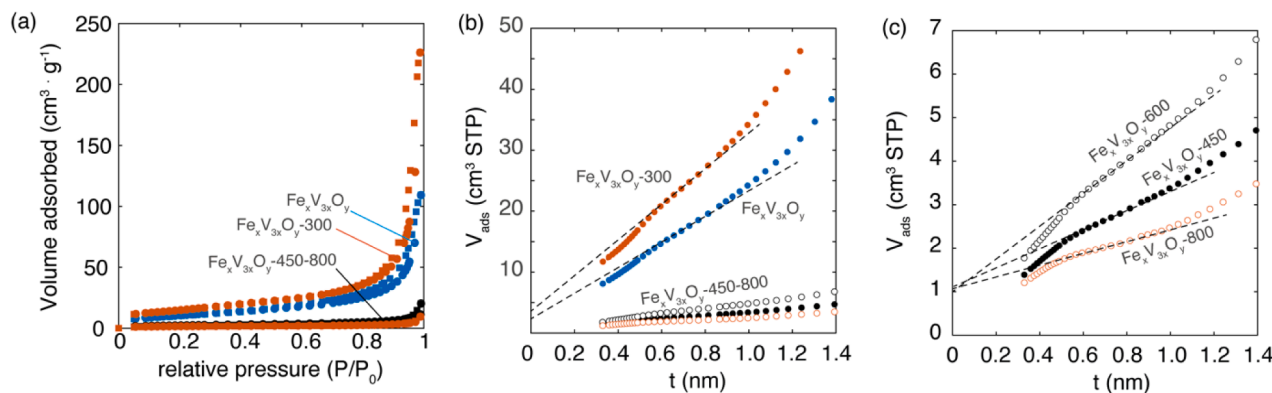


Fig. 5. t-plot analysis from N₂ adsorption isotherm of Fe_xV_{3x}O_y·zH₂O, Fe_xV_{3x}O_y-T (300–800 °C).

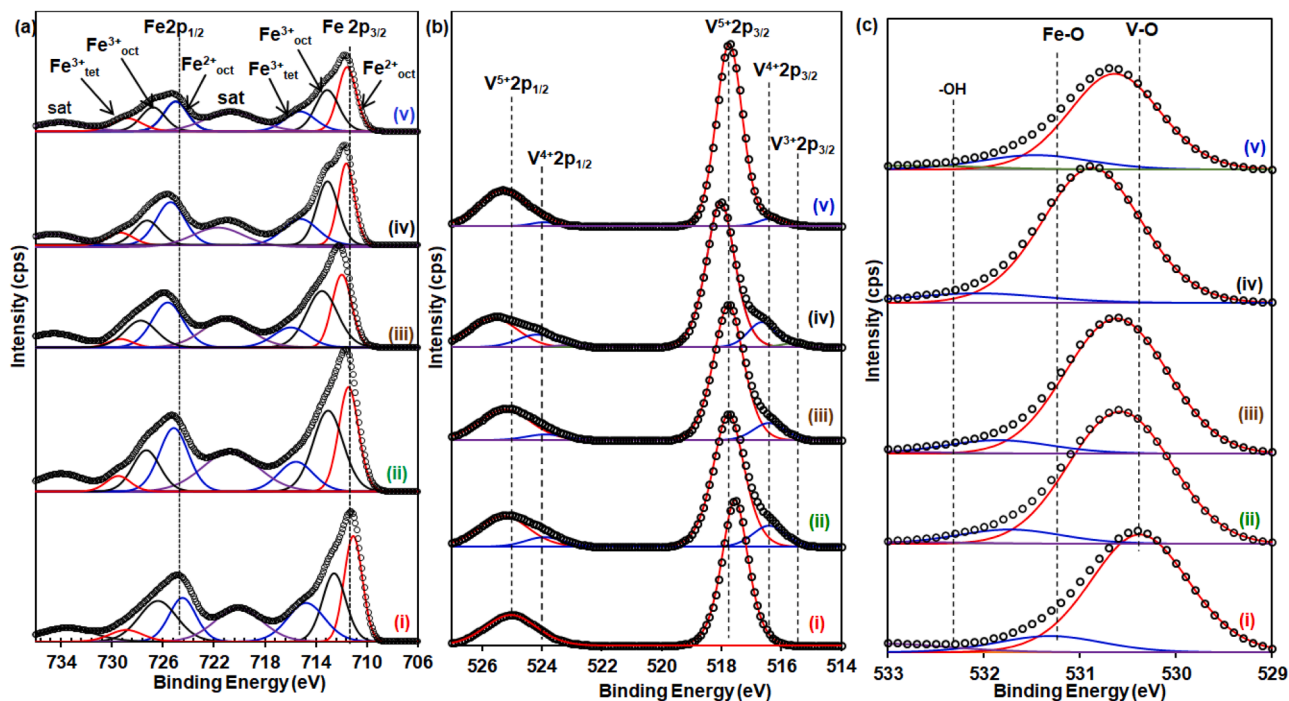


Fig. 6. High-resolution core-level spectra of (a) Fe 2p, (b) V 2p, and (c) O 1s for (i) Fe_xV_{3x}O_y·zH₂O, (ii) Fe_xV_{3x}O_y-300, (iii) Fe_xV_{3x}O_y-450, (iv) Fe_xV_{3x}O_y-600 and (v) Fe_xV_{3x}O_y-800.

between +0.6 and +1.1 V was observed for both FA and MTX at the bare SPC electrode (Fig. 7a), indicating the slow kinetics of MTX and FA electrooxidation. However, the CVs of SPC/Fe_xV_{3x}O_y·zH₂O and all the SPC/Fe_xV_{3x}O_y-T electrodes showed a well-resolved anodic peak at -0.75 V for FA and -0.90 V for MTX (Fig. 7, b-f). No cathodic peak was observed, confirming the irreversibility of FA and MTX oxidation at the bare SPC and SPC/Fe_xV_{3x}O_y-T modified electrodes. The well-resolved redox peaks and higher current response confirmed the electrocatalytic activity of Fe_xV_{3x}O_y-T towards the oxidation of MTX and FA. The anodic peak currents density for FA and MTX electrooxidation at all calcined Fe_xV_{3x}O_y-T modified SPC electrodes was significantly higher than the Fe_xV_{3x}O_y·zH₂O modified SPC electrodes (Fig.S9). It could be inferred that the formation of low valency state (Fe²⁺, V³⁺, and V⁴⁺) species and oxygen vacancies defects during calcination facilitated MTX and FA electrooxidation. The defect sites could facilitate the adsorption of MTX and FA onto the surface of the dehydrated Fe_xV_{3x}O_y-T. The MTX and FA anodic current density varied with the Fe_xV_{3x}O_y-T calcination temperatures.

The MTX and FA anodic current density varied with the Fe_xV_{3x}O_y-T

calcination temperatures. The Fe_xV_{3x}O_y-300 and Fe_xV_{3x}O_y-450 had the highest peak current density for FA and MTX (Fig.S9). This is attributed to the higher electroactive surface area, mesoporosity, and higher electron transfer kinetics of Fe_xV_{3x}O_y-450. Based on these findings, Fe_xV_{3x}O_y-450 was chosen for further electrochemical studies.

The effects of pH on the electrocatalytic oxidation of FA (pK₁ = 3.1, carboxylic acid; pK₂ = 4.8, pK₃ = 10.4, amines) and MTX (pK₁ = 4.7, carboxylic acid; pK₂ = 8.8, pK₃ = 9.2, amine) at the SPC/Fe_xV_{3x}O_y-450 was investigated. The anodic peak potential of MTX shifted towards a more negative value with increasing pH from 3.0 to 5.0 as MTX species underwent deprotonation (Fig. S10, a). In contrast, at pH ≥ 6.0, the oxidation of MTX was not dependent on the pH as the MTX became fully deprotonated. The electrooxidation of MTX at the SPC/Fe_xV_{3x}O_y-450 electrode involves the transfer of electrons and a protons abstraction process [34,35]. The plot of the anodic potential against the pH of MTX is linear in the ranges of 3.0 < pH < 6.0 with a regression equation E_{pa}(V) = 1.04 - 0.028 pH (R² = 0.985, Fig.S10 (a')). The obtained slope of 28 mV per pH unit was about half of the theoretical Nernst value (59 mV/pH), indicating that the ratio of electron transfers to proton

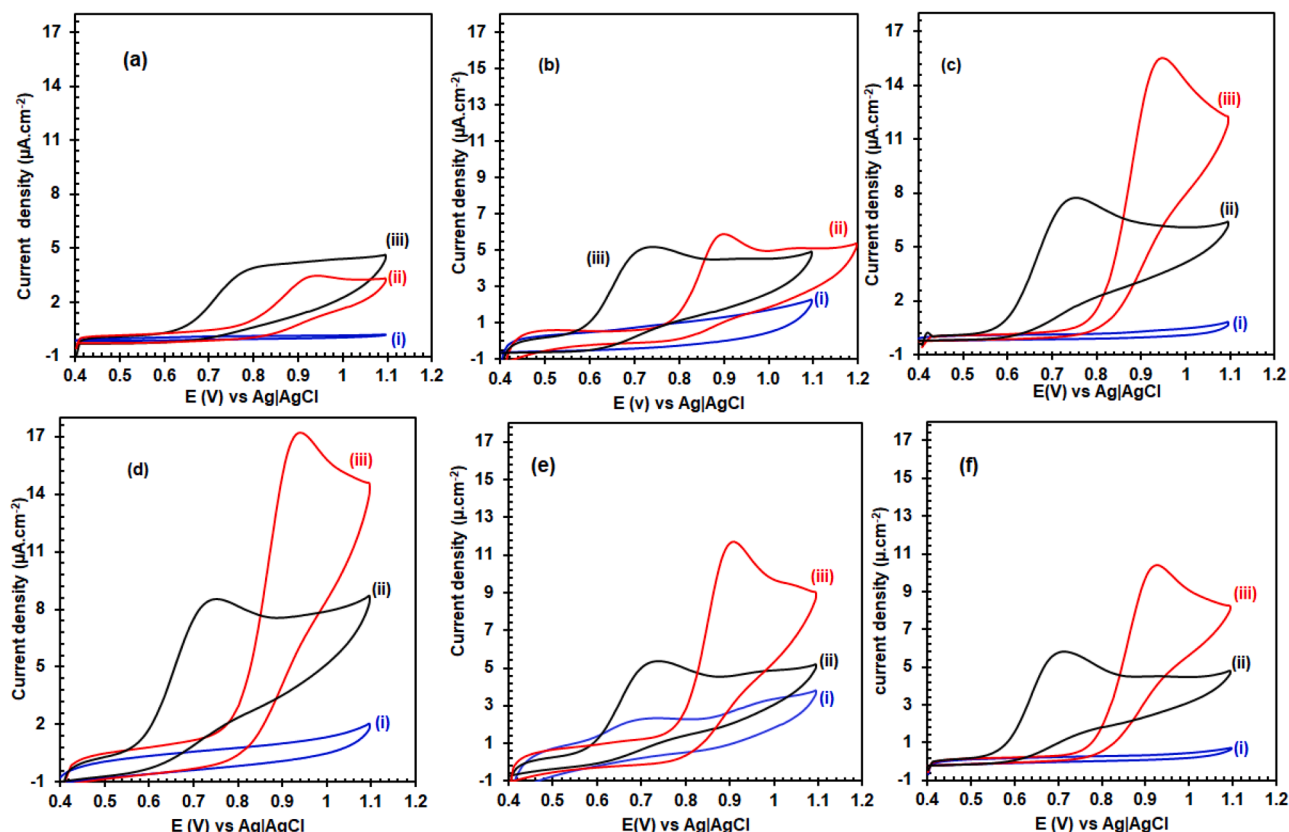


Fig. 7. CVs of (a) SPCE, (b) SPC/Fe_xV_{3x}O_y.zH₂O, (c) SPC/Fe_xV_{3x}O_y-300, (d) SPC/Fe_xV_{3x}O_y-450, (e) SPC/Fe_xV_{3x}O_y-600 and (f) SPC/Fe_xV_{3x}O_y-800 electrode in the (i) PBS (ii) 50 μM of FA and (iii) 50 μM of MTX in PBS (pH 7.0) at 50 mV.s⁻¹.

abstraction involved in the electrooxidation of MTX at the SPC/Fe_xV_{3x}O_y-450 electrode was 0.5. The CVs of FA at the SPC/Fe_xV_{3x}O_y-450 showed two anodic peaks (*I_a* and *I_a'*) in the pH range 3.0 < pH ≤ 6.0 (Fig. S10, b). The second anodic peak (*I_a'*) was not observed in the CVs of FA at neutral and basic pH (≥ 7.0). The first anodic peak potential (*I_a* = 0.72 V) at pH 3.0 shifted linearly to a more negative potential (*I_a* = 0.65 V) at pH 6.0, while there was a shift to a more positive value at pH ≥ 7.0. The linear regression equation of potential against pH was *E_{pl_a}* = 0.79 - 0.023 pH at pH ≤ 6.0 and *E_{pl_a}* = -0.70 - 0.012 pH at pH ≥ 7.0 (Fig. S10, b'). The ratio of proton to electron transfer involved in the oxidation of FA at the SPC/Fe_xV_{3x}O_y-450 is 0.5 at pH ≤ 6.0. The mechanism of electrooxidation of FA at acidic and alkali pH has previously been documented in the literature [36,37]. It could be seen that the second anodic peak (*I_a'*) of FA overlaps with the anodic peak (*I_a*) of MTX in the pH ranges of 3.0 ≤ pH ≤ 5.0. The overlap of the (*I_a'*) peak of FA with the anodic peak of MTX would complicate the accurate determination of MTX in the presence of FA at pH ≤ 5.0. Therefore, pH 7.0, where the second anodic peak (*I_a'*) of FA is absent, was selected to quantitatively determine MTX and FA at the SPC/Fe_xV_{3x}O_y-450 electrodes.

The electrooxidation of MTX and FA at the SPC/Fe_xV_{3x}O_y-450 electrode in PBS (pH 7.0) was investigated by changing the CV scan rate from 5 to 150 mV/s. The anodic current density of MTX and FA increases, and the potential shifts to more positive values with an increasing scan rate from 10 to 150 mV.s⁻¹ (Fig. S11). The anodic peak current of FA and MTX were linearly proportional to the scan rate in the studied ranges (Fig. S11, a' and b'). The linearity indicated that the oxidation of FA and MTX at the SPC/Fe_xV_{3x}O_y-450 is an adsorption-controlled process, demonstrating that MTX and FA are adsorbed onto the active sites of Fe_xV_{3x}O_y-450 and are electrooxidized. The differential pulse voltammetry (DPV) of SPC/Fe_xV_{3x}O_y-450 for repeated measurement of MTX (Fig. S12a) showed a decrease in the current response with an increasing number of DPV repetitive scans. The observed current

density decrease is attributed to the adsorption of oxidized MTX product onto the active sites of the SPC/Fe_xV_{3x}O_y-450 electrode. This is a characteristic behavior of the adsorption-controlled oxidation mechanism [38]. Fig. S12 (b) showed that a simple rinsing step with PBS solution between each successive run of MTX could remove the adsorbed byproduct and restore the baseline signal (Fig. S12b) to achieve repeated use. There were no differences in the current response to a repetitive measurement of 50.0 μM of MTX even after the 10th measurement, confirming good repeatability and reusability. The reaction time of SPC/Fe_xV_{3x}O_y-450 with MTX was optimized using 50 μM of MTX. The current density increases with increasing reaction time up to 5 min, after which there was no significant increase in the peak current response. Hence, 5 min without applying a preconcentration potential was used for the measurements.

3.4. Voltammetric detection of MTX and FA using SPC/Fe_xV_{3x}O_y-450

Differential pulse voltammetry (DPV) was used to determine the level of MTX and FA in PBS and human blood serum samples under the optimized conditions. The anodic current density increased with increasing concentrations of FA (Fig. 8a) and MTX (Fig. 8b). The analytical calibration curve was established from the plot of change in the current density ($\Delta I = I_a - I_0$) before (*I₀*) and after MTX or FA interaction (*I_a*). The linear concentration range was from 0.05 to 200 μM with a regression equation of $\Delta I = 0.473[\text{FA}] (\mu\text{M}) + 16.84$ (*R*² = 0.982) for FA (Fig. 8c) and from 0.005 to 200 μM with a regression equation $\Delta I = 1.249 [\text{MTX}] (\mu\text{M}) + 14.42$ (*R*² = 0.995) for MTX (Fig. 8d). The detection limit (LoD) and quantification (LoQ) were estimated from a multiplier of 3σ/sensitivity and 10σ/sensitivity, respectively. There was no appreciable current increase without MTX and FA, and the background signal's standard deviation (σ) was 4.04 (*n* = 6). The LoD and LoQ were 2.85 nM and 9.83 nM, respectively, for MTX and 7.79 and

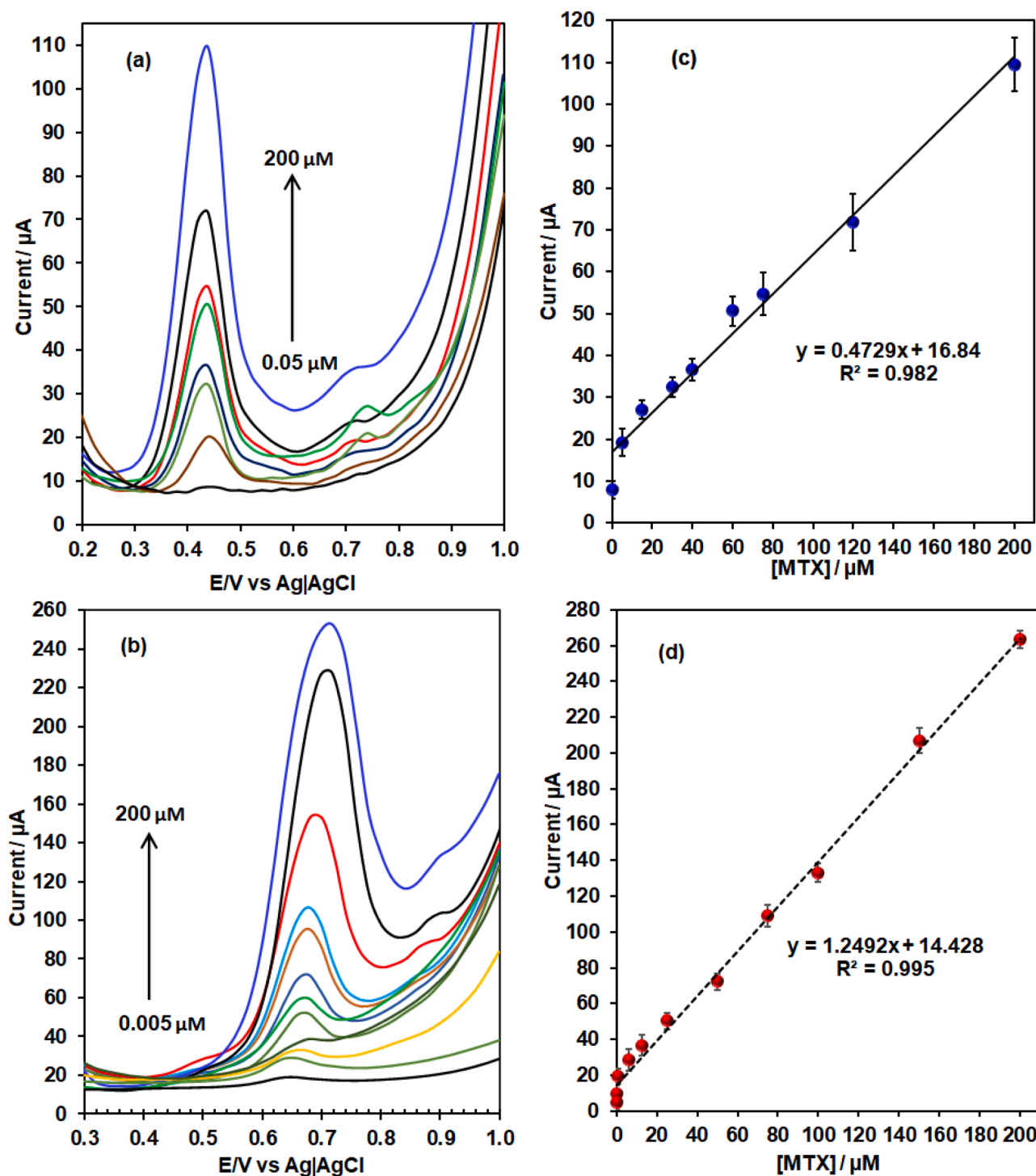


Fig. 8. DPV of (a) MTX and (b) FA at the SPC/Fe_xV_{3x}O_y-450 electrode and the corresponding linear calibration plot of current density against (c) MTX concentrations and (d) FA concentrations in PBS (pH 7.0).

25.9 nM, respectively, for FA. The comparison of the linear range and LoD of SPC/Fe_xV_{3x}O_y-450 with previously reported MTX and FA sensing systems are summarized in Table 1. The SPC/Fe_xV_{3x}O_y-450 showed the limit of detections for FA and MTX in the low nM range, comparable to the other reported sensing systems. However, the SPC/Fe_xV_{3x}O_y-450 had the advantage of detecting MTX in a wider linear range (0.005 to 200 μM) compared to previously reported voltammetric sensing systems. Although the linear range of our previously reported AuE/anti-MTX_{Ab} (0.0002 - 270) in ref. [4] and GCE-IPA/anti-MTX_{Ab} (0.0003 - 300) in ref. [5] are considerably wider than SPC/Fe_xV_{3x}O_y-450 (0.005 to

200 μM), it should be noted that these methods are based on very expensive and easily denatured antibodies, and simultaneous determination of MTX and FA has not been possible. The linear range and the LoD of the SPC/Fe_xV_{3x}O_y-450 are within the clinically targeted MTX concentrations of 5.0 to 10.0 μM at 24 h, 0.10 μM at 72 h, and 0.05 μM at 96 h after intravenous MTX administration [39], which makes it possible to measure MTX and FA in blood serum without dilution.

Table 1
Comparison of SPC/Fe_xV_{3x}O_y-450 with other electroanalytical methods.

Electrode Material	Method	Linear range (μM)	LOD (nM)	Refs
SPC/Fe _x V _{3x} O _y -450	DPV	^a 0.005 – 200 ^b 0.50 – 200	^a 2.95 ^b 7.79	TW
AuE/anti-MTX antibody	EIS	^a 0.0002 – 270	^a 0.165	[4]
GCE-IPA/anti-MTX antibody	EIS	^a 0.0003 – 300	^a 0.007	[5]
SPC/V ₂ O ₅ @g-C ₃ N ₄	DPV	^a 0.025 – 273.15	^a 13.3	[40]
GCE/Q-MWCNTs/PABSA	DPV	^a 0.1 – 80 ^b 0.1 – 6.5	^b 15.0 ^a 20.0	[41]
GCE/SWCNT/Nafion/DNA	DPV	^a 0.02 – 1.5	^a 8.0	[42]
SPGE/PPY/Pd/Fe ₃ O ₄	DPV	^a 0.03–100	^a 7.0	[43]
GCE/NiONS	DPV	^a 0.5 – 30	^a 1.45	[44]
GCE-Nafion-GO	DPV	^a 40 – 200	^a 9.0	[38]
GCE/ZnO–Ce	DPV	^a 0.01 – 500	^a 6.3	[45]
CPE/F-CNTPE	DPV	^a 0.40 – 5.5	^a 2.9	[46]

^a MTX and ^b FA sensors. (TW – this work), EIS: Electrochemical impedance spectroscopy-multivariate data analysis; DPV: differential pulse voltammetry.

3.5. Simultaneous determination of MTX in the presence of FA

To test the applicability of the SPC/Fe_xV_{3x}O_y-450 electrode for monitoring MTX and FA in human clinical samples, human serum was spiked with concentrations of MTX (0.05 – 5.0 μM) and FA (0.5 – 40 μM) within the clinically relevant concentration ranges. The SPC/Fe_xV_{3x}O_y-450 electrode did not show an appreciable current response in the serum samples, indicating endogenous electroactive serum constituents are not oxidized within the studied potential window. The DPV of the mixed FA

and MTX spiked blood serum in Fig. 9(a) showed two well-resolved anodic peaks at 550 and 798 mV corresponding to the irreversible electrooxidation of FA and MTX, respectively. The peak separation between the FA and MTX signal was 248 mV, demonstrating that the SPC/Fe_xV_{3x}O_y-450 electrode can detect MTX and FA in a mixed solution without signal overlap. The current response increases simultaneously with increasing concentrations of both MTX and FA in the spiked blood serum samples (Fig. 9a). An appreciable current response was observed at low concentrations of MTX (≤ 0.05) in the serum samples. However, the response was recorded at higher concentrations of FA (≥ 0.5), probably due to the higher sensitivity of SPC/Fe_xV_{3x}O_y-450 for MTX than FA. The linear regression equation for the simultaneous quantification was $\Delta I_p = 1.279[\text{MTX}] (\mu\text{M}) + 1.55$ ($R^2 = 0.998$), within a linear dynamic range of 0.05 to 5.0 μM of MTX and $\Delta I_p = 0.118[\text{FA}] (\mu\text{M}) + 1.117$ ($R^2 = 0.992$) for the linear range of 0.50 to 40 μM of FA. The DPV of the mixed solutions of 10.0 μM of FA with different concentrations of MTX from 0.5 to 3.0 μM (Fig S13) showed the current response due to the MTX increases with increasing MTX concentrations, while the current response due to FA did not change significantly (Fig S13). This confirmed that the SPC/Fe_xV_{3x}O_y-450 sensor could detect lower concentrations of MTX in the presence of a higher concentration of FA without a signal crosstalk effect. The precision of the SPC/Fe_xV_{3x}O_y-450 was evaluated using an inter-assay of human serum samples spiked with 0.05, 0.10, and 0.20 μM of MTX and 0.5, 1.0, and 2.0 μM of FA. The recovery concentrations were evaluated from the calibration plot in Fig. 9(b) and 9(c). The percentage recoveries (Table S5) were between 93.5 and 104.6% for MTX and 99.5 to 105% for FA, demonstrating that the SPC/Fe_xV_{3x}O_y-450 sensor has good precision for monitoring MTX

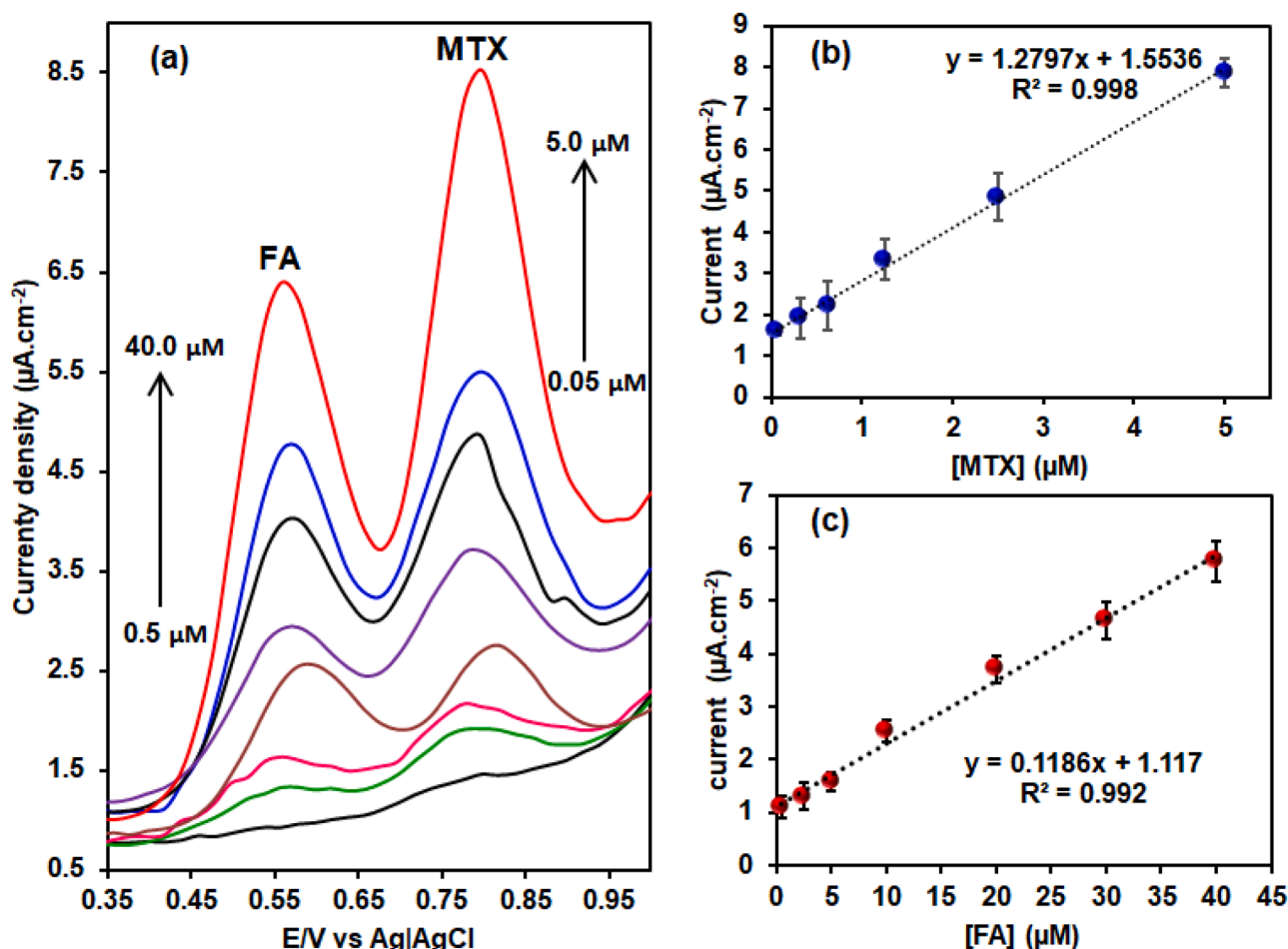


Fig. 9. (a) DPV of different standard concentrations of MTX and FA in blood serum and the corresponding calibration plot of change in current density against different (b) MTX and (c) FA concentrations.

and FA in blood serum samples. The SPC/Fe_xV_{3x}O_y-450 electrode could selectively and accurately detect MTX in a mixed solution of both analytes without interference.

The selectivity of the SPC/Fe_xV_{3x}O_y-450 for MTX and FA in the presence of other electroactive endogenous serological substances, such as dopamine (DOP), ascorbic acid (AA), glucose (Glu), tetrahydrofolic acid (HFA) and uric acid (UA). The interferent substances showed no voltammetric response within the examined potential range (0.5–1.0 V), Fig. S14. The peak current of the mix of FA, MTX, and the interfering substances did not change significantly, demonstrating the good anti-interference properties of SPC/Fe_xV_{3x}O_y-450.

4. Conclusions

In summary, various kazakhstanite-like layered iron vanadate (Fe_xV_{3x}O_y) were synthesized via coprecipitation followed by calcination at different temperatures. The morphology, crystallinity, electronic bandgap, and redox activity of the Fe_xV_{3x}O_y changed with the calcination temperature. Electrochemical experimental studies showed that the Fe_xV_{3x}O_y calcinated at 450 °C had excellent electrocatalytic performance towards the electrooxidation of methotrexate (MTX) and folic acid (FA). The enhanced electrocatalytic performance of SPC/Fe_xV_{3x}O_y-450 was attributed to the layered nanoflake morphology, higher electroactive surface area, and nanoporosity. The oxidation of MTX and FA at the SPC/Fe_xV_{3x}O_y-450 is an adsorption-controlled process. The SPC/Fe_xV_{3x}O_y-450 electrode demonstrated a low detection limit with a wide linear range compared to previously reported detection methods. The SPC/Fe_xV_{3x}O_y-450 could detect MTX and FA in human blood serum samples without signal crosstalk and interferences from endogenous serum protein, demonstrating its potential for monitoring the level of MTX during chemotherapy.

CRedit authorship contribution statement

Kayode Omotayo Adeniyi: Conceptualization, Methodology, Data curation, Writing – original draft. **Blerina Osmanaj:** Methodology, Validation, Writing – review & editing. **Gopinathan Manavalan:** Methodology, Validation, Writing – review & editing. **Ajaikumar Samikannu:** Writing – review & editing. **Jyri-Pekka Mikkola:** Conceptualization, Supervision, Resources, Writing – review & editing, Funding acquisition. **Berisha Avni:** Writing – review & editing. **Jean-François Boily:** Conceptualization, Supervision, Resources, Writing – review & editing, Funding acquisition. **Solomon Tesfalidet:** Conceptualization, Supervision, Resources, Writing – review & editing, Funding acquisition.

Declaration of Competing Interest

The authors declare that they have no known competing financial interests or personal relationships that could have appeared to influence the work reported in this paper.

Data availability

No data was used for the research described in the article.

Acknowledgments

This research was funded by the Kempe Foundations. We thank Bio4Energy, a Strategic Research Environment appointed by the Swedish government, for supporting this work. The Umeå center for Electron Microscopy (UCEM) and Vibrational Spectroscopy Core Facility (ViSp) at the Chemical Biological center (KBC), Umeå University, is gratefully acknowledged.

Supplementary materials

Supplementary material associated with this article can be found, in the online version, at [doi:10.1016/j.electacta.2023.142538](https://doi.org/10.1016/j.electacta.2023.142538).

References

- [1] Y.M. Salamoun, K. Polireddy, Y.K. Cho, M.R. Medcalf, R.S. Funk, Methotrexate disposition, anti-folate activity, and metabolomic profiling to identify molecular markers of disease activity and drug response in the collagen-induced arthritis mouse model, *Metabolites* 12 (2022) 1–17, <https://doi.org/10.3390/metabo12010024>.
- [2] P. Joannon, I. Oviedo, M. Campbell, J. Tordecilla, High-dose methotrexate therapy of childhood acute lymphoblastic leukemia: lack of relation between serum methotrexate concentration and creatinine clearance, *Pediatr. Blood Cancer* 43 (2004) 17–22, <https://doi.org/10.1002/pbc.20032>.
- [3] R. Niinimäki, H. Aarnivala, J. Banerjee, T. Pokka, K. Vepsäläinen, A. Harila-Saari, Reduced dose folinic acid rescue after rapid high-dose methotrexate clearance is not associated with increased toxicity in a pediatric cohort, *Support. Care Cancer* 30 (2022) 127–133, <https://doi.org/10.1007/s00520-021-06395-3>.
- [4] S. Tesfalidet, P. Geladi, K. Shimizu, B. Lindholm-Sethson, Detection of methotrexate in a flow system using electrochemical impedance spectroscopy and multivariate data analysis, *Anal. Chim. Acta* 914 (2016) 1–6, <https://doi.org/10.1016/j.aca.2016.02.012>.
- [5] D. Mwanza, S. Phal, T. Nyokong, S. Tesfalidet, P. Mashazi, Electrografting of isophthalic acid monolayer and covalent attachment of antibody onto carbon surfaces: construction of capacitive biosensor for methotrexate detection, *Electrochim. Acta* 398 (2021), 139360, <https://doi.org/10.1016/j.electacta.2021.139360>.
- [6] S. Phal, B. Shatri, A. Berisha, P. Geladi, B. Lindholm-Sethson, S. Tesfalidet, Covalently electrografted carboxyphenyl layers onto gold surface serving as a platform for the construction of an immunosensor for detection of methotrexate, *J. Electroanal. Chem.* 812 (2018) 235–243, <https://doi.org/10.1016/j.jelechem.2017.12.072>.
- [7] N. Baig, A. Rana, A.N. Kawde, Modified electrodes for selective voltammetric detection of biomolecules, *Electroanalysis* 30 (2018) 2551–2574, <https://doi.org/10.1002/elan.201800468>.
- [8] A. Chowdhury, R. Shukla, V. Sharma, S. Neogy, A. Chandra, V. Grover, A.K. Tyagi, Controlling reaction kinetics of layered zinc vanadate having brucite-like Zn–O layers supported by pyrovanadate pillars for use in supercapacitors, *J. Alloys Compd.* 829 (2020), 154479, <https://doi.org/10.1016/j.jallcom.2020.154479>.
- [9] J. Kim, S.H. Lee, C. Park, H.S. Kim, J.H. Park, K.Y. Chung, H. Ahn, Controlling vanadate nanofiber interlayer via intercalation with conducting polymers: cathode material design for rechargeable aqueous zinc ion batteries, *Adv. Funct. Mater.* (2021) 31, <https://doi.org/10.1002/adfm.202100005>.
- [10] G. Kesavan, M. Pichumani, S.M. Chen, Influence of crystalline, structural, and electrochemical properties of iron vanadate nanostructures on flutamide detection, *ACS Appl. Nano Mater.* 4 (2021) 5883–5894, <https://doi.org/10.1021/acsanm.1c00802>.
- [11] G. Kesavan, P.K. Gopi, S.M. Chen, V. Vinothkumar, Iron vanadate nanoparticles supported on boron nitride nanocomposite: electrochemical detection of antipsychotic drug chlorpromazine, *J. Electroanal. Chem.* 882 (2021), 114982, <https://doi.org/10.1016/j.jelechem.2021.114982>.
- [12] U. Rajaji, K. Yogesh Kumar, S.M. Chen, M.S. Raghu, L. Parashuram, F.M. Alzahrani, N.S. Alsaari, M. Ouladmane, Deep eutectic solvent synthesis of iron vanadate-decorated sulfur-doped carbon nanofiber nanocomposite: electrochemical sensing tool for doxorubicin, *Microchim. Acta* (2021) 188, <https://doi.org/10.1007/s00604-021-04950-7>.
- [13] E. Israel, H. Resolution, T. Electron, Catalysis science of methanol oxidation over iron vanadate catalysts, *ACS Catal.* 1 (2011) 54–66.
- [14] G. Kesavan, M. Pichumani, S.M. Chen, C.J. Wu, Hydrothermal synthesis of iron vanadate nanoparticles for voltammetric detection of antipsychotic drug thioridazine, *J. Alloys Compd.* 885 (2021), 160880, <https://doi.org/10.1016/j.jallcom.2021.160880>.
- [15] Z. Peng, Q. Wei, S. Tan, P. He, W. Luo, Q. An, L. Mai, Novel layered iron vanadate cathode for high-capacity aqueous rechargeable zinc batteries, *Chem. Commun.* 54 (2018) 4041–4044, <https://doi.org/10.1039/c8cc00987b>.
- [16] M.S. Chae, D. Setiawan, H.J. Kim, S.T. Hong, Layered iron vanadate as a high-capacity cathode material for nonaqueous calcium-ion batteries, *Batteries* 7 (2021) 1–9, <https://doi.org/10.3390/batteries7030054>.
- [17] Q. Wei, Q. Wang, Q. Li, Q. An, Y. Zhao, Z. Peng, Y. Jiang, S. Tan, M. Yan, L. Mai, Pseudocapacitive layered iron vanadate nanosheets cathode for ultrahigh-rate lithium-ion storage, *Nano Energy* 47 (2018) 294–300, <https://doi.org/10.1016/j.nanoen.2018.02.028>.
- [18] R.C. Singh, M.P. Singh, O. Singh, P.S. Chandi, Influence of synthesis and calcination temperatures on particle size and ethanol sensing behavior of chemically synthesized SnO₂ nanostructures, *Sens. Actuators B Chem.* 143 (2009) 226–232, <https://doi.org/10.1016/j.snb.2009.09.032>.
- [19] M.B. Rammal, V. El-Ghoubaira, S. Omani, I.I. Part, NiMoO₄ nanostructures synthesized by the solution combustion method: a parametric study on the influence of material synthesis and electrode-fabrication parameters on the electrocatalytic activity in the hydrogen evolution reaction, *Molecules* (2022) 27, <https://doi.org/10.3390/molecules27041199>.

- [20] B. Saravanakumar, N. Karthikeyan, P.A. Periasamy, A.J. Britten, M. Mkandawire, Polyethylene glycol mediated synthesis of iron vanadate (FeVO_4) nanoparticles with supercapacitive features, *Mater. Res. Express* 7 (2020), <https://doi.org/10.1088/2053-1591/ab997f>.
- [21] S.A. Mahmoud, S.H. Bendary, A.A. Salem, O.A. Fouad, Facile synthesis of high yield two-dimensional zinc vanadate nanoflakes, *SN Appl. Sci.* 1 (2019) 1–8, <https://doi.org/10.1007/s42452-019-0508-2>.
- [22] A.Š. Vuk, B. Orel, G. Drazić, F. Decker, P. Colomban, UV-visible and IR spectroelectrochemical studies of FeVO_4 sol-gel films for electrochromic applications, *J. Sol Gel Sci. Technol.* 23 (2002) 165–181, <https://doi.org/10.1023/A:1013755618889>.
- [23] F.N.I. Sari, S. Abdillah, J.M. Ting, FeOOH -containing hydrated layered iron vanadate electrocatalyst for superior oxygen evolution reaction and efficient water splitting, *Chem. Eng. J.* 416 (2021), 129165, <https://doi.org/10.1016/j.cej.2021.129165>.
- [24] Y. Dong, D. Zhang, D. Li, H. Jia, W. Qin, Control of Ostwald ripening, *Sci. China Mater.* 66 (2022) 1249–1255, <https://doi.org/10.1007/s40843-022-2233-3>.
- [25] M. Wang, Y. Shi, G. Jiang, 3D hierarchical $\text{Zn}_3(\text{OH})_2\text{V}_2\text{O}_7 \cdot 2\text{H}_2\text{O}$ and $\text{Zn}_3(\text{VO}_4)_2$ microspheres: synthesis, characterization and photoluminescence, *Mater. Res. Bull.* 47 (2012) 18–23, <https://doi.org/10.1016/j.materresbull.2011.10.020>.
- [26] F. Ambroz, T.J. Macdonald, V. Martis, I.P. Parkin, Evaluation of the BET theory for the characterization of meso and microporous MOFs, *Small Methods* 2 (2018) 1–17, <https://doi.org/10.1002/smt.201800173>.
- [27] S. Brunauer, P.H. Emmett, E. Teller, Adsorption of gases in multimolecular layers, *J. Am. Chem. Soc.* 60 (1938) 309–319, <https://doi.org/10.1021/ja01269a023>.
- [28] D.D. Do, *Adsorption Analysis: Equilibria and Kinetics*, Imperial College Press, London, 1998.
- [29] A. Kumar, T. Shripathi, P.C. Srivastava, New insights into CoFe/n-Si interfacial structure as probed by X-ray photoelectron spectroscopy, *J. Sci. Adv. Mater. Devices* 1 (2016) 290–294, <https://doi.org/10.1016/j.jsamd.2016.07.008>.
- [30] A.P. Grosvenor, B.A. Kobe, M.C. Biesinger, N.S. McIntyre, Investigation of multiplet splitting of $\text{Fe}2p$ XPS spectra and bonding in iron compounds, *Surf. Interface Anal.* 36 (2004) 1564–1574, <https://doi.org/10.1002/sia.1984>.
- [31] W. Yang, G. Tan, J. Huang, H. Ren, A. Xia, C. Zhao, Enhanced magnetic property and photocatalytic activity of UV-light responsive N-doped $\text{Fe}_2\text{O}_3/\text{FeVO}_4$ heterojunction, *Ceram. Int.* 41 (2015) 1495–1503, <https://doi.org/10.1016/j.ceramint.2014.09.084>.
- [32] X. Zhao, Y. Yan, L. Mao, M. Fu, H. Zhao, L. Sun, Y. Xiao, G. Dong, A relationship between the $\text{V}^{4+}/\text{V}^{5+}$ ratio and the surface dispersion, surface acidity, and redox performance of $\text{V}_2\text{O}_5\text{-WO}_3/\text{TiO}_2$ SCR catalysts, *RSC Adv.* 8 (2018) 31081–31093, <https://doi.org/10.1039/c8ra02857e>.
- [33] A.M.O.B.C. Brett, *Electrochemistry - Principles, methods, and Applications*, 98, Oxford Univ. Press, Oxford, 1993, <https://doi.org/10.1002/bbpc.19940981033>, 1350–1350.
- [34] A.D.R. Pontinha, S.M.A. Jorge, V.C. Diculescu, M. Vivan, A.M. Oliveira-Brett, Antineoplastic drug methotrexate redox mechanism using a glassy carbon electrode, *Electroanalysis* 24 (2012) 917–923, <https://doi.org/10.1002/elan.201100558>.
- [35] J. Li, D. Chen, T. Zhang, G. Chen, Highly sensitive electrochemical determination of methotrexate based on an N-doped hollow nanocarbon sphere modified electrode, *Anal. Methods* 13 (2021) 117–123, <https://doi.org/10.1039/d0ay01996h>.
- [36] A. Taherkhani, T. Jamali, H. Hadadzadeh, H. Karimi-Maleh, H. Beitollahi, M. Taghavi, F. Karimi, ZnO nanoparticle-modified ionic liquid-carbon paste electrode for voltammetric determination of folic acid in food and pharmaceutical samples, *Ionics* 20 (2014) 421–429, <https://doi.org/10.1007/s11581-013-0992-0> (Kiel).
- [37] S. Akbar, A. Anwar, Q. Kanwal, Electrochemical determination of folic acid: a short review, *Anal. Biochem.* 510 (2016) 98–105, <https://doi.org/10.1016/j.ab.2016.07.002>.
- [38] D. Huang, H. Wu, Y. Zhu, H. Su, H. Zhang, L. Sheng, Z. Liu, H. Xu, C. Song, Sensitive determination of anticancer drug methotrexate using graphite oxide-Nafion modified glassy carbon electrode, *Int. J. Electrochem. Sci.* 14 (2019) 3792–3804, <https://doi.org/10.20964/2019.04.03>.
- [39] X. Shi, H. Gao, Z. Li, J. Li, Y. Liu, L. Li, Q. Zhang, Modified enzyme multiplied immunoassay technique of methotrexate assay to improve sensitivity and reduce cost, *BMC Pharmacol. Toxicol.* 20 (2019) 1–7, <https://doi.org/10.1186/s40360-018-0283-5>.
- [40] T.W. Chen, U. Rajaji, S.M. Chen, B.S. Lou, N. Al-Zaqri, A. Alsalmeh, F.A. Alharthi, S. Y. Lee, W.H. Chang, A sensitive electrochemical determination of chemotherapy agent using graphitic carbon nitride covered vanadium oxide nanocomposite; sonochemical approach, *Ultrason. Sonochem.* 58 (2019), 104664, <https://doi.org/10.1016/j.ultrasonch.2019.104664>.
- [41] Z. Zhu, F. Wang, F. Wang, L. Xi, Simultaneous determination of methotrexate and calcium folinate with an electrochemical method based on a poly-ABSA/functionalized MWNTs composite film modified electrode, *J. Electroanal. Chem.* 708 (2013) 13–19, <https://doi.org/10.1016/j.jelechem.2013.09.004>.
- [42] F. Wang, Y. Wu, J. Liu, B. Ye, Electrochimica Acta DNA Langmuir–Blodgett modified glassy carbon electrode as voltammetric sensor for determination of methotrexate, *Electrochim. Acta* 54 (2009) 1408–1413, <https://doi.org/10.1016/j.electacta.2008.09.027>.
- [43] S. Tajik, H. Beitollahi, S. Shahsavari, F.G. Nejad, Simultaneous and selective electrochemical sensing of methotrexate and folic acid in biological fluids and pharmaceutical samples using $\text{Fe}_3\text{O}_4/\text{ppy}/\text{Pd}$ nanocomposite modified screen printed graphite electrode, *Chemosphere* 291 (2022), 132736, <https://doi.org/10.1016/j.chemosphere.2021.132736>.
- [44] A.A. Khand, S.A. Lakho, A. Tahira, M. Ubaidullah, A.A. Alothman, K. Aljada, A. Nafady, Z.H. Ibupoto, Facile electrochemical determination of methotrexate (MTX) using glassy carbon electrode-modified with electronically disordered NiO nanostructures, *Nanomaterials* (2021) 11, <https://doi.org/10.3390/nano11051266>.
- [45] N. Jandaghi, S. Jahani, M.M. Foroughi, M. Kazemipour, M. Ansari, Cerium-doped flower-shaped ZnO nano-crystallites as a sensing component for simultaneous electrochemical determination of epirubicin and methotrexate, *Microchim. Acta* (2020) 187, <https://doi.org/10.1007/s00604-019-4016-2>.
- [46] S. Kummari, V.S. Kumar, M. Satyanarayana, K.V. Gobi, Direct electrochemical determination of methotrexate using functionalized carbon nanotube paste electrode as a biosensor for *in-vitro* analysis of urine and dilute serum samples, *Microchem. J.* 148 (2019) 626–633, <https://doi.org/10.1016/j.microc.2019.05.054>.